

# New Iron-Based Mixed-Polyanion Cathodes for Lithium and Sodium Rechargeable Batteries: Combined First Principles Calculations and Experimental Study

Hyungsub Kim,<sup>†,‡,#</sup> Inchul Park,<sup>†,#</sup> Dong-Hwa Seo,<sup>†</sup> Seongsu Lee,<sup>‡</sup> Sung-Wook Kim,<sup>†</sup> Woo Jun Kwon,<sup>§</sup> Young-Uk Park,<sup>†</sup> Chul Sung Kim,<sup>§</sup> Seokwoo Jeon,<sup>||</sup> and Kisuk Kang<sup>\*,†</sup>

<sup>†</sup>Department of Materials Science and Engineering, Research Institute of Advanced Materials, Seoul National University, 599 Gwanak-ro, Gwanak-gu, Seoul 151-742, Republic of Korea

<sup>‡</sup>Korea Atomic Energy Research Institute, P.O. Box 105, Yuseong-gu, Daejeon 305-600, Republic of Korea

<sup>§</sup>Department of Physics, Kookmin University, Seoul 136-702, Republic of Korea

<sup>||</sup>Department of Materials Science and Engineering, KAIST, 291 Daehak-ro, Yuseong-gu, Daejeon 305-600, Republic of Korea

## S Supporting Information

**ABSTRACT:** New iron-based mixed-polyanion compounds  $\text{Li}_x\text{Na}_{4-x}\text{Fe}_3(\text{PO}_4)_2(\text{P}_2\text{O}_7)$  ( $x = 0-3$ ) were synthesized, and their crystal structures were determined. The new compounds contained three-dimensional (3D)-sodium/lithium paths supported by  $\text{P}_2\text{O}_7$  pillars in the crystal. First principles calculations identified the complex 3D paths with their activation barriers and revealed them as fast ionic conductors. The reversible electrode operation was found in both Li and Na cells with capacities of one-electron reaction per Fe atom, 140 and 129 mAh  $\text{g}^{-1}$ , respectively. The redox potential of each phase was  $\sim 3.4$  V (vs Li) for the Li-ion cell and  $\sim 3.2$  V (vs Na) for the Na-ion cell. The properties of high power, small volume change, and high thermal stability were also recognized, presenting this new compound as a potential competitor to other iron-based electrodes such as  $\text{Li}_2\text{FeP}_2\text{O}_7$ ,  $\text{Li}_2\text{FePO}_4\text{F}$ , and  $\text{LiFePO}_4$ .

An integral part of the new energy economy is to provide cost-effective, sustainable energy storage. Chemical energy storage in the form of batteries, in particular, the most advanced lithium-ion batteries, will contribute strongly to the energy storage picture. However, the cost-effectiveness per energy and the safety hazards regarding lithium-ion batteries have so far prohibited their widespread use in large-scale applications.

In this respect, the search for new polyanion compounds using iron as a redox center is of timely significance. Using naturally abundant iron as a full redox couple, combined with stabilization of the oxygen atoms within the crystal via the strong covalent bonds of the polyanion,<sup>1</sup> may significantly reduce the energy costs and safety concerns. This has led to the use of olivine lithium iron phosphate,  $\text{LiFePO}_4$ , as a popular cathode material for lithium-ion batteries.<sup>2,3</sup> Recent studies on polyanion materials using the  $\text{Fe}^{2+}/\text{Fe}^{3+}$  redox couple have identified new compounds, such as fluorinated iron phosphate ( $\text{Li}_2\text{FePO}_4\text{F}$ ),<sup>4</sup> iron pyrophosphate ( $\text{Li}_2\text{FeP}_2\text{O}_7$ ),<sup>1,5</sup> fluorinated iron sulfate ( $\text{LiFeSO}_4\text{F}$ ),<sup>6,7</sup> iron silicate ( $\text{Li}_2\text{FeSiO}_4$ ),<sup>8</sup> and iron borate ( $\text{LiFeBO}_3$ ),<sup>9,10</sup> as alternatives. However, the synthesis of

fluorinated compounds requires complex and costly procedures, and their theoretical capacities are hardly obtainable. Moreover, some of the fluorinated compounds such as  $\text{Li}_2\text{FePO}_4\text{F}$  are moisture sensitive, while the most moisture stable phase is  $\text{LiFePO}_4\text{F}$ .<sup>11,12</sup> Lithium iron silicates and iron borates are unable to provide sufficient voltage, and the specific capacity of  $\text{Li}_2\text{FeP}_2\text{O}_7$  is less than 110 mAh  $\text{g}^{-1}$ .

In the search for new iron-based lithium-containing cathode materials, our prime interest is in mixed-polyanion systems, which were examined by pioneering work of Goodenough et al.<sup>13,14</sup> Recently, mixed-polyanion compounds are refocused, and theoretical work predicted that the combination of  $\text{YO}_3^{2-}$  or  $3-$  and  $\text{XO}_4^{3-}$  or  $4-$  ( $Y = \text{C}, \text{B}$ ;  $X = \text{Si}, \text{As}, \text{P}$ ) could give a series of new  $\text{A}_x\text{M}(\text{YO}_3)(\text{XO}_4)$  compounds ( $A = \text{Li}, \text{Na}$ ;  $M =$  a redox transition metal; and  $x = 0-3$ ) suitable for cathode materials.<sup>15,16</sup> The experimental synthesis of the mixed-phosphate,  $\text{Li}_3\text{V}_3(\text{P}_2\text{O}_7)_3(\text{PO}_4)_2$ , with the vanadium  $\text{V}^{3+}/\text{V}^{5+}$  redox couple, showed promising electrochemical properties.<sup>17,18</sup> We believe that the variety of combinations among different polyanion groups may lead to the discovery of a new open crystal framework containing both lithium and iron.

One of our main objectives of this study was to synthesize materials based on the mixed polyanion groups of  $(\text{PO}_4)^{3-}$  and  $(\text{P}_2\text{O}_7)^{4-}$  with the  $\text{Fe}^{2+}/\text{Fe}^{3+}$  redox couple. Currently, the known mixed phosphate that is closest to our aim is  $\text{Na}_4\text{Me}_3(\text{PO}_4)_2(\text{P}_2\text{O}_7)$  ( $\text{Me} = \text{Mn}, \text{Co}, \text{Ni}, \text{Mg}$ ).<sup>19,20</sup> However, to the best of our knowledge, an iron analogue with this composition has been neither synthesized nor documented in the materials database. It was expected that such an unreported compound would not be stable under conventional synthesis conditions, and may, therefore, require a special synthesis route. However, contrary to expectations,  $\text{Na}_4\text{Fe}_3(\text{PO}_4)_2(\text{P}_2\text{O}_7)$  was easily obtained using a simple solid-state method. Furthermore, from the first principles calculations, we found  $\text{Na}_4\text{Fe}_3(\text{PO}_4)_2(\text{P}_2\text{O}_7)$  to be a promising candidate for cathode materials in terms of its voltage and the mobility of alkali cations for Na-ion batteries. Finally, we showed that sodium

Received: April 23, 2012

Published: June 5, 2012

could be topotactically ion-exchanged with lithium to produce a new lithium compound that inherited the good electrochemical properties of the parent sodium phase for lithium-ion batteries.

$\text{Na}_4\text{Fe}_3(\text{PO}_4)_2(\text{P}_2\text{O}_7)$  was successfully synthesized via a conventional solid-state reaction at 500 °C (see Supporting Information, experimental section and Figure S1). Figure 1a

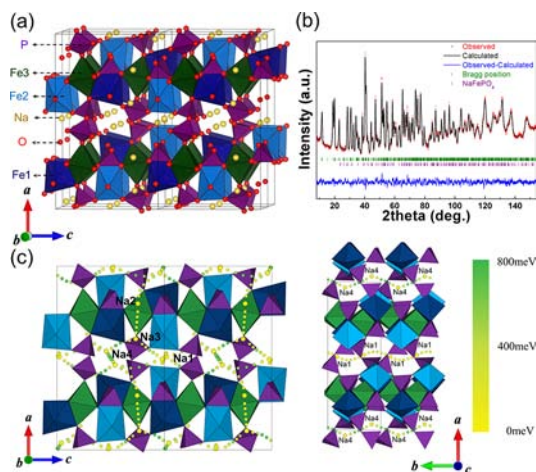


**Figure 1.** (a) Schematic representation of  $\text{Na}_4\text{Fe}_3(\text{PO}_4)_2(\text{P}_2\text{O}_7)$ . (b) Rietveld refinement of the neutron diffraction patterns of  $\text{Na}_4\text{Fe}_3(\text{PO}_4)_2(\text{P}_2\text{O}_7)$ . The observed and calculated intensities are represented by the red markers and the black solid line, respectively. The bottom blue line represents the difference between the observed and calculated patterns. Bragg positions for  $\text{Na}_4\text{Fe}_3(\text{PO}_4)_2(\text{P}_2\text{O}_7)$  are represented as green markers, and the  $\text{NaFePO}_4$  (~4%) impurity is shown as purple markers. (c) The 3D sodium diffusion paths in the  $\text{Na}_4\text{Fe}_3(\text{PO}_4)_2(\text{P}_2\text{O}_7)$  structure. The yellow circles indicate four Na-ion sites; the purple tetrahedra represent phosphate; the blue, cyan, and green octahedra represent iron (Fe1, Fe2, and Fe3, respectively). For clarity, the oxygen ions are not shown. The color gradient from yellow to green on the smaller Na circles represents the site energies of Na during path migration, which allows visualization of the activation barriers.

shows a schematic representation of the crystal. The crystal framework is composed of a 3D network of  $[\text{Fe}_3\text{P}_2\text{O}_{13}]_\infty$

infinite layers parallel to the  $b-c$  plane. The  $[\text{Fe}_3\text{P}_2\text{O}_{13}]_\infty$  layer is connected along the  $a$ -axis by  $\text{P}_2\text{O}_7$  groups, and this diphosphate connection produces large tunnels that can provide one of the Na-diffusion channels along the  $b$ -axis. The structural characterization based on neutron diffraction (ND) data, shown in Figure 1b, confirmed that the  $\text{Na}_4\text{Fe}_3(\text{PO}_4)_2(\text{P}_2\text{O}_7)$  is isostructural to  $\text{Na}_4\text{Co}_3(\text{PO}_4)_2(\text{P}_2\text{O}_7)$ , as reported by Sanz et al.<sup>16</sup> The Rietveld refinement with a space group of  $Pn2_1a$  identified that  $a = 18.07517$  (7) Å,  $b = 6.53238$  (2) Å,  $c = 10.64760$  (4) Å, and  $V = 1257.204$  (1) Å<sup>3</sup>. The fitting was satisfactory ( $R_p = 1.92\%$ ,  $R_l = 1.98\%$ ,  $R_f = 1.01\%$ ). A detailed structural illustration of  $\text{Na}_4\text{Fe}_3(\text{PO}_4)_2(\text{P}_2\text{O}_7)$  and a summary of the crystal data can be found in Figure S2 and Table S1. A trace amount (<4%) of the  $\text{NaFePO}_4$  impurity was detected in the ND patterns, and the impurity formation gradually increased above 550 °C, as shown by *in situ* high-temperature X-ray diffraction (XRD) analysis (Figure S3), thermal gravimetric analysis (TGA), and differential scanning calorimetry (DSC) results (Figure S1).

There are four symmetrically distinguishable Na sites in the crystal, and these are connected to each other throughout the 3D framework. Two Na sites (Na2 and Na3) formed by seven coordinated  $\text{NaO}_7$  polyhedra and  $\text{NaO}_6$  octahedra are present along the  $a$ -axis. Two other Na sites (Na1 and Na4), formed by  $\text{NaO}_6$  octahedra, are located on the  $b-c$  plane, as shown in Figure 1c. All of the probable diffusion pathways among the four Na sites were examined by first principles calculations. Figure 1c illustrates the only energetically plausible Na diffusion paths, with activation barriers lower than 800 meV. The color gradient from yellow to green in Figure 1c indicates the site energies of Na during the migration along the path, from which we can identify the fast diffusion pathways of Na. While all Na sites are connected with reasonably low activation barriers, the Na diffusion in the large tunnel along the  $b$ -axis (Na1–Na1) shows the lowest activation barrier (see Table S2 for the activation barriers for each Na diffusion path). The Na moves sinusoidally along the  $b$ -axis due to the electrostatic repulsion from the neighboring iron, as shown in Figure S4b. It is interesting to note that the sinusoidal motion of Li along the 1D channel was also observed in  $\text{LiFePO}_4$ .<sup>21</sup> Figure S4 shows

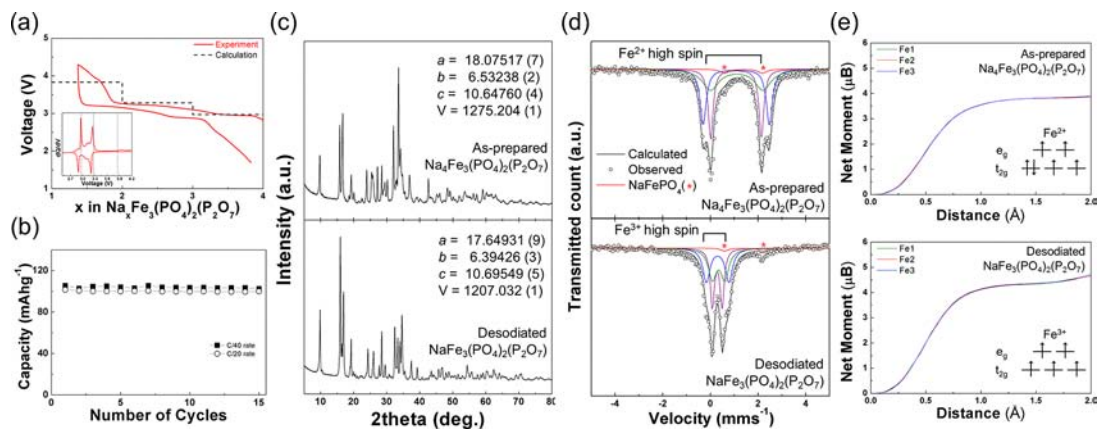


**Figure 2.** (a) Galvanostatic charge/discharge profiles of  $\text{Na}_4\text{Fe}_3(\text{PO}_4)_2(\text{P}_2\text{O}_7)$  under a C/40 rate and the calculated average voltage at each region. The inset shows the  $dQ/dV$  curve of initial charge/discharge profiles. (b) Cycle performance of a Na cell under C/40 and C/20 rates. (c) XRD patterns and (d) Mössbauer spectra of  $\text{Na}_x\text{Fe}_3(\text{PO}_4)_2(\text{P}_2\text{O}_7)$  ( $x = 1, 4$ ). Observed and calculated patterns are present as black circles and lines, respectively, in Mössbauer spectrum. The blue, green, and purple lines represent the three distinct iron sites. The red line shows the  $\text{Fe}^{2+}$  component in the  $\text{NaFePO}_4$  impurity; this peak does not change during the desodiation process. (e) Integrated spin as a function of integration radius around Fe in  $\text{Na}_{4-x}\text{Fe}_3(\text{PO}_4)_2(\text{P}_2\text{O}_7)$  ( $x = 0, 3$ ).

the detailed diffusion mechanism and the landscape of the activation barrier.

Inspired by the feasible Na diffusion in the crystal, the electrochemical properties of  $\text{Na}_4\text{Fe}_3(\text{PO}_4)_2(\text{P}_2\text{O}_7)$  were tested in a Na cell. The Na cell was fabricated with  $\text{Na}_4\text{Fe}_3(\text{PO}_4)_2(\text{P}_2\text{O}_7)$  as the cathode, a sodium counter-electrode as the anode, and  $\text{NaClO}_4$  in propylene carbonate (PC) as the electrolyte. Figure 2a shows the voltage trace as a function of sodium composition for  $\text{Na}_x\text{Fe}_3(\text{PO}_4)_2(\text{P}_2\text{O}_7)$  with a 4.3 V cutoff voltage in a Na cell. About 88% of the theoretical capacity which can be considered as one electron reaction per Fe atom was obtained at the rate of C/40, with an average voltage of  $\sim 3.2$  V. The electrochemical activity centered around 3.2 V is consistent with the theoretical prediction of the voltage from the first principles calculations, as indicated in Figure 2a. It is noted that unusually high polarization is observable at the end of the first charge profile. We speculate that this phenomenon can be related to the local structural change occurring around the Na tunnels at the end of the charge. The examination of the structural evolution from first principles calculation reveals that  $\text{P}_2\text{O}_7$  dimer that constitutes the Na diffusion tunnels in the structure significantly distorts at  $1 \leq x \leq 2$  in  $\text{Na}_x\text{Fe}_3(\text{PO}_4)_2(\text{P}_2\text{O}_7)$ , while the precise relation between  $\text{P}_2\text{O}_7$  dimer distortion and the Na mobility is currently under investigation. Relatively good cycle performance was observed at both the C/40 rate and C/20 rate, as shown in Figure 2b.

The mechanism by which sodium is extracted from  $\text{Na}_4\text{Fe}_3(\text{PO}_4)_2(\text{P}_2\text{O}_7)$  was studied by monitoring Mössbauer spectra and XRD patterns of  $\text{Na}_4\text{Fe}_3(\text{PO}_4)_2(\text{P}_2\text{O}_7)$  and fully charged  $\text{NaFe}_3(\text{PO}_4)_2(\text{P}_2\text{O}_7)$ . Figure 2c indicates that the comparison of the XRD patterns of the two samples did not show a significant change; this implies a topotactical de/insertion of the sodium ions. However, a change in the lattice parameters was observed. The values of  $a$ ,  $b$ , and the volume decreased when the three sodium ions were extracted, while the  $c$  lattice parameter increased significantly.

The volume change was less than 4%, which is considerably low compared with other cathode materials.<sup>3,4,6</sup> The lattice parameters of each phase are tabulated in Table S3 along with the ND analysis, which showed the same trend. The comparison of Mössbauer spectra of the two samples clearly indicated that the  $\text{Fe}^{2+}/\text{Fe}^{3+}$  redox reaction mainly accompanies the de/sodiation shown in Figure 2d. Mössbauer analysis in Figure 2d confirmed that most of the iron in  $\text{Na}_4\text{Fe}_3(\text{PO}_4)_2(\text{P}_2\text{O}_7)$  initially existed as  $\text{Fe}^{2+}$ . The blue, green, and purple lines in Mössbauer spectra represent the three distinct iron sites. The values of the quadruple splitting ( $\Delta E_Q$ ) and isomer shift ( $IS$ ) are in good agreement with those observed in other  $\text{Fe}^{2+}$ -containing compounds.<sup>22</sup> However, when a full charge of  $\text{Na}_4\text{Fe}_3(\text{PO}_4)_2(\text{P}_2\text{O}_7)$  is complete, resulting in the formation of  $\text{NaFe}_3(\text{PO}_4)_2(\text{P}_2\text{O}_7)$ , the  $\Delta E_Q$  and  $IS$  shift toward values typically observed for  $\text{Fe}^{3+}$ . A trace amount of  $\text{Fe}^{2+}$  detected was attributed to the  $\text{NaFePO}_4$  impurity, consistent with the ND study. This result agrees with the first principles calculation of the Fe valence states for the two samples. The spin integration around Fe indicates that the valence of Fe is +2 for the as-prepared sample and +3 for the charged sample, as shown in Figure 2e. Detailed information on  $\Delta E_Q$ , the  $IS$  values, and the iron site ratios are provided in Table S4.

The thermal phase stability of the charged electrode is one of the indicators that determine the safety characteristics of the battery at elevated temperatures. The charged electrode,

$\text{NaFe}_3(\text{PO}_4)_2(\text{P}_2\text{O}_7)$ , was further investigated using TGA/DSC measurements and *in situ* high-temperature XRD. TGA/DSC analyses indicate that the desodiated phase was stable up to 500 °C, with only  $\sim 4\%$  weight loss (see Figure S5). An exothermic peak was observed around 530 °C, where the decomposition into  $\text{NaFeP}_2\text{O}_7$  and  $\text{Fe}_2\text{P}_2\text{O}_7$  was detected from the *in situ* high-temperature XRD results (see Figure S6). The high stability of the  $\text{NaFe}_3(\text{PO}_4)_2(\text{P}_2\text{O}_7)$  was comparable to that of charged olivine  $\text{LiFePO}_4$  and pyrophosphate  $\text{Li}_2\text{FeP}_2\text{O}_7$ ,<sup>3,5</sup> presenting intrinsically safe characteristics of polyanion-compound electrodes.

The lithium analogue of  $\text{Na}_4\text{Fe}_3(\text{PO}_4)_2(\text{P}_2\text{O}_7)$  was produced via a topotactic ion-exchange of the Na cation to the Li cation within the lattice by refluxing in a solution of LiBr. Three Na ions were successfully replaced by Li ions in the lattice, while one Na remained in the structure, resulting in the production of  $\text{Li}_3\text{NaFe}_3(\text{PO}_4)_2(\text{P}_2\text{O}_7)$ . The Li/Na composition was confirmed to be 3.06:0.9 by inductively coupled plasma-atomic emission spectroscopy (ICP-AES). Figure 3a shows the XRD

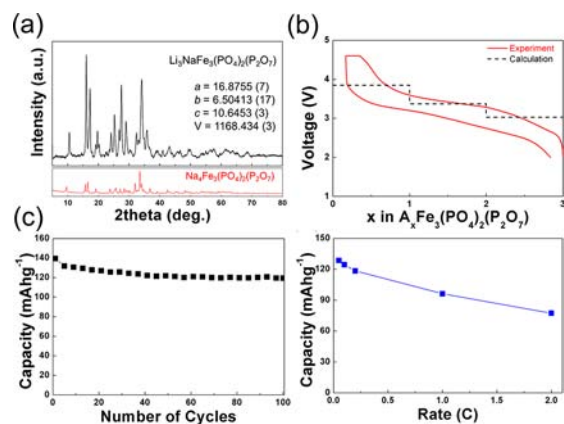


**Figure 3.** (a) XRD patterns of  $\text{Li}_3\text{NaFe}_3(\text{PO}_4)_2(\text{P}_2\text{O}_7)$ . The reference sodium phase of  $\text{Na}_4\text{Fe}_3(\text{PO}_4)_2(\text{P}_2\text{O}_7)$  is represented below. (b) Calculated voltage and galvanostatic charge/discharge profiles of the Li cell under a C/20 rate at 298 K and calculated voltage profiles; (c) cyclability of the Li-ion cell under C/5 at 333 K. (d) The rate capability of  $\text{Li}_3\text{NaFe}_3(\text{PO}_4)_2(\text{P}_2\text{O}_7)$  in the Li-ion cell. In the case of the Li-ion cell, a second cycle is shown for profile clarity.

patterns of  $\text{Li}_3\text{NaFe}_3(\text{PO}_4)_2(\text{P}_2\text{O}_7)$ . The general patterns are similar to those of  $\text{Na}_4\text{Fe}_3(\text{PO}_4)_2(\text{P}_2\text{O}_7)$ , implying that the crystal framework was maintained. However, the lattice parameters were determined to be smaller,  $a = 16.8755$  (7) Å,  $b = 6.50413$  (17) Å, and  $c = 10.6453$  (3) Å, for  $\text{Li}_3\text{NaFe}_3(\text{PO}_4)_2(\text{P}_2\text{O}_7)$  from profile matching, due in part to the smaller ionic radius of Li compared with Na. In particular, a significant reduction of the  $a$  lattice was observed. We believe that the replacement of Na with Li in the  $(\text{Na}1)\text{O}_6$  and  $(\text{Na}4)\text{O}_6$  polyhedra located on the  $b$ - $c$  plane caused a significant distortion of the  $\text{P}_2\text{O}_7$  pillars, which induced the collapse of the interlayer spacing along the  $a$ -axis.

Electrochemical measurements on the Li-ion cell were performed with a Li metal anode in a 2016-type coin cell at 298 and 333 K. Figure 3b shows the voltage-lithium composition trace of  $\text{Li}_3\text{NaFe}_3(\text{PO}_4)_2(\text{P}_2\text{O}_7)$ . It should be noted that the electrochemical cycling of  $\text{Li}_3\text{NaFe}_3(\text{PO}_4)_2(\text{P}_2\text{O}_7)$  electrode did not show any noticeable change in Na contents. This implies that residual Na may play a role of pillar in the structure. Nevertheless, we believe that

various environments such as different C-rates, cutoff voltages, and particle sizes can affect the sodium contents in the structure of  $\text{Li}_3\text{NaFe}_3(\text{PO}_4)_2(\text{P}_2\text{O}_7)$ . About 92% of the theoretical capacity was obtained at a C/20 rate with an average voltage of 3.4 V. The electrochemical activity centered around 3.4 V agrees with the voltage trace predicted from the first principles calculations, as indicated in Figure 3b. The average voltage of the  $\text{Li}_3\text{NaFe}_3(\text{PO}_4)_2(\text{P}_2\text{O}_7)$  is only slightly higher than that of  $\text{Na}_4\text{Fe}_3(\text{PO}_4)_2(\text{P}_2\text{O}_7)$ . It is attributed to the relative instability of Li ions in the crystal framework which is derived from a parent Na-phase. Relatively good cycle performance was observed, as shown Figure 3c. Almost 86% of the initial discharge capacity was retained at 333 K after 100 cycles. The battery operation at higher current densities showed that ~75% of the initial capacity could be delivered in 1 h (1C rate) and ~60% even in 30 min (2C rate), suggesting that this electrode could sustain respectable rate capabilities (see Figure 3d). Note that this electrode was fabricated without any special efforts such as carbon-coating or nanosizing, and there exists about 4% inactive  $\text{NaFePO}_4$  impurity. We believe that further synthesis optimization can improve the electrochemical properties significantly. The excellent rate capability and cycle performance was attributed to the open and stable polyanion framework of the electrode material. The open framework is beneficial for fast ion transport, but may, in turn, sacrifice the volumetric energy density for practical use. Nevertheless, comparison with other iron-based polyanion cathodes reported so far showed that the volumetric energy density of  $\text{Li}_3\text{NaFe}_3(\text{PO}_4)_2(\text{P}_2\text{O}_7)$  is comparable to them as tabulated in Table S5.

In conclusion, new mixed-polyanion-based compounds,  $\text{Li}_x\text{Na}_{4-x}\text{Fe}_3(\text{PO}_4)_2(\text{P}_2\text{O}_7)$  ( $x = 0, 3$ ), were successfully synthesized, and their energy densities were 380 and 460 Wh  $\text{kg}^{-1}$  in sodium- and lithium-ion batteries, respectively. The respectable cathode activity in both sodium- and lithium-ion batteries was delivered without special efforts, such as carbon-coating or nanosizing. The combined  $(\text{PO}_4)^{3-}$  and  $(\text{P}_2\text{O}_7)^{4-}$  polyanion groups, which provided a new crystal framework that accommodated the naturally abundant Fe redox center and lithium/sodium ions, exhibited stable and fast cathode activity in lithium and sodium batteries. The emerging rich chemistry in mixed-polyanion materials suggests that significant opportunity exists to explore new low-cost, high-performance electrodes in this class of materials.

## ■ ASSOCIATED CONTENT

### Supporting Information

Experimental sections, TGA/DSC analyses, detailed structural information, *in situ* high temperature XRD patterns of  $\text{Na}_x\text{Fe}_3(\text{PO}_4)_2(\text{P}_2\text{O}_7)$  ( $x = 1, 4$ ), detailed structural schematics of the  $\text{Na}_4\text{Fe}_3(\text{PO}_4)_2(\text{P}_2\text{O}_7)$ . This material is available free of charge via the Internet at <http://pubs.acs.org>.

## ■ AUTHOR INFORMATION

### Corresponding Author

matlgen1@snu.ac.kr

### Author Contributions

#These authors contributed equally.

### Notes

The authors declare no competing financial interest.

## ■ ACKNOWLEDGMENTS

This work was supported by Human Resources Development of the KETEP (20114010203120) and from the World Premier Materials grant funded by the Korean Ministry of Knowledge Economy. This work was also supported by the National Research Foundation of Korea (NRF-2009-0094219) and Mid-career Researcher Program (2012-0000169) funded by the Ministry of Education, Science and Technology (MEST). The calculation resources were supported by the Supercomputing Center in KISTI (KSC-2011-C2-51).

## ■ REFERENCES

- (1) Nishimura, S.; Nakamura, M.; Natsui, R.; Yamada, A. *J. Am. Chem. Soc.* **2010**, *132* (39), 13596–13597.
- (2) Padhi, A. K.; Nanjundaswamy, K.; Goodenough, J. B. *J. Electrochem. Soc.* **1997**, *144* (4), 1188–1194.
- (3) Delacourt, C.; Poizot, P.; Tarascon, J.-M.; Masquelier, C. *Nat. Mater.* **2005**, *4*, 254–260.
- (4) Ellis, B. L.; Makahnouk, W. R.; Makimura, Y.; Toghiani, K.; Nazar, L. F. *Nat. Mater.* **2007**, *6* (10), 749–753.
- (5) Kim, H.; Lee, S.; Park, Y.-U.; Kim, H.; Kim, J.; Jeon, S.; Kang, K. *Chem. Mater.* **2011**, *23* (17), 3930–3937.
- (6) Recham, N.; Chotard, J.-N.; Dupont, L.; Delacourt, C.; Walker, W.; Armand, M.; Tarascon, J.-M. *Nat. Mater.* **2009**, *9* (1), 68–74.
- (7) Barpanda, P.; Ati, M.; Melot, B. C.; Rousse, G.; Chotard, J. N.; Doublet, M. L.; Sougrati, M. T.; Corr, S.-A.; Jumas, J. C.; Tarascon, J. M. *Nat. Mater.* **2011**, *10* (10), 772–779.
- (8) Nyten, A.; Abouimrane, A.; Armand, M.; Gustafsson, T.; Thomas, J. O. *Electrochem. Commun.* **2005**, *7* (2), 156–160.
- (9) Yamada, A.; Iwane, N.; Harada, Y.; Nishimura, S.; Koyama, Y.; Tanaka, I. *Adv. Mater.* **2010**, *22* (32), 3583–3587.
- (10) Seo, D.-H.; Park, Y.-U.; Kim, S.-W.; Park, I.; Shakoor, R.; Kang, K. *Phys. Rev. B* **2011**, *83*, 205127–1–8.
- (11) Ramesh, T. N.; Lee, K. T.; Ellis, B. L.; Nazar, L. F. *Electrochem. Solid-State Lett.* **2010**, *13* (4), A43–A47.
- (12) Ellis, B. L.; Ramesh, T. N.; Rowan-Weetaluktuk, W. N.; Ryan, D. H.; Nazar, L. F. *J. Mater. Chem.* **2012**, *22*, 4759–4766.
- (13) Padhi, A. K.; Nanjundaswamy, K. S.; Masquelier, C.; Okada, S.; Goodenough, J. B. *J. Electrochem. Soc.* **1997**, *144* (5), 1609–1613.
- (14) Padhi, A. K.; Manivannan, V.; Goodenough, J. B. *J. Electrochem. Soc.* **1998**, *145* (5), 1518–1520.
- (15) Hautier, G.; Jain, A.; Chen, H.; Moore, C.; Ong, S. P.; Ceder, G. *J. Mater. Chem.* **2011**, *21* (43), 17147–17153.
- (16) Jain, A.; Hautier, G.; Moore, C.; Kang, B.; Lee, J.; Chen, H.; Twu, N.; Ceder, G. *J. Electrochem. Soc.* **2012**, *159* (5), 622–633.
- (17) Kuang, Q.; Xu, J.; Zhao, Y.; Chen, X.; Chen, L. *Electrochim. Acta* **2011**, *56* (5), 2201–2205.
- (18) Kuang, Q.; Lin, Z.; Zhao, Y.; Chen, X.; Chen, L. *J. Mater. Chem.* **2011**, *21* (38), 14760–14765.
- (19) Sanz, F.; Parada, C.; Rojo, J.; Ruiz-Valero, C. *Chem. Mater.* **2001**, *13* (4), 1334–1340.
- (20) Essehli, R.; Bali, E. B.; Benmokhtar, S.; Fuess, H.; Svoboda, I.; Obbade, Said. *J. Alloys Compd.* **2010**, *493* (1), 654–660.
- (21) Nishimura, S.; Kobayashi, G.; Ohoyama, K.; Kanno, R.; Yashima, M.; Yamada, A. *Nat. Mater.* **2008**, *7*, 707–711.
- (22) Andersson, A.-S.; Kalska, B.; Häggström, L.; Thomas, J.-O. *Solid State Ionics* **2000**, *130* (1), 41–52.